Geophysical Research Letters

RESEARCH LETTER
10.1029/2022GL101232

Key Points:

- Reflection of solar wind protons from lunar regolith is simulated with SDTrimSP-3D
- A precise agreement with spacecraft measurements of energetic neutral atom emission is only found for highly porous regolith structures
- A lunar regolith porosity of $0.85^{+0.15}_{-0.14}$ is derived from solar wind proton reflection, which could also be applied to other airless bodies

Supporting Information:

Supporting Information may be found in the online version of this article.

Correspondence to:

P. S. Szabo,
szabo@berkeley.edu

Citation:

Szabo, P. S., Poppe, A. R., Biber, H., Mutzke, A., Pichler, J., Jäggi, N., et al. (2022). Deducing lunar regolith porosity from energetic neutral atom emission. *Geophysical Research Letters*, *49*, e2022GL101232. https://doi.org/10.1029/2022GL101232

Received 9 SEP 2022
Accepted 19 OCT 2022

Author Contributions:

Conceptualization: P. S. Szabo, A. R. Poppe, N. Jäggi, A. Galli, P. Wurz, F. Aumayr
Data curation: P. S. Szabo
Formal analysis: P. S. Szabo
Funding acquisition: A. R. Poppe, F. Aumayr
Investigation: P. S. Szabo
Methodology: P. S. Szabo, H. Biber
Project Administration: A. R. Poppe, F. Aumayr
Resources: A. Galli, P. Wurz
Software: P. S. Szabo, H. Biber, A. Mutzke, J. Pichler
Supervision: A. R. Poppe, A. Galli, F. Aumayr
Validation: P. S. Szabo, A. R. Poppe
Visualization: P. S. Szabo
Writing – original draft: P. S. Szabo

Deducing Lunar Regolith Porosity From Energetic Neutral Atom Emission

P. S. Szabo[1], A. R. Poppe[1], H. Biber[2], A. Mutzke[3], J. Pichler[2], N. Jäggi[4], A. Galli[4], P. Wurz[4], and F. Aumayr[2]

[1]Space Sciences Laboratory, University of California, Berkeley, CA, USA, [2]Institute of Applied Physics, TU Wien, Vienna, Austria, [3]Max Planck Institute for Plasma Physics (IPP), Greifswald, Germany, [4]Physics Institute, University of Bern, Bern, Switzerland

Abstract The porosity of the upper layers of regolith is key to the interaction of an airless planetary body with precipitating radiation, but it remains difficult to characterize. One of the effects that is governed by regolith properties is Energetic Neutral Atom (ENA) emission in the form of reflected and neutralized solar wind protons. We simulate this process for the surface of the Moon by implementing a regolith grain stacking in the ion-solid-interaction software SDTrimSP-3D, finding that proton reflection significantly depends on the regolith porosity. Via comparison with ENA measurements by Chandrayaan-1, we derive a globally averaged porosity of the uppermost regolith layers of $0.85^{+0.15}_{-0.14}$. These results indicate a highly porous, fairy-castle-like nature of the upper lunar regolith, as well as its importance for the interaction with impacting ions. Our simulations further outline the possibility of future regolith studies with ENA measurements, for example, by the BepiColombo mission to Mercury.

Plain Language Summary The Moon's surface is covered with regolith, a soil made up of stacked grains. Properties of this regolith influence how the Moon interacts with its environment. One example of such an effect are impact by charged particles emitted from the Sun called the "solar wind." We now present simulations of the reflection of such particles from the surface of the Moon, taking into account the grain structure of the regolith. We only find an agreement between the simulations and spacecraft measurements of reflected solar wind particles for very loosely stacked grains. Overall, the amount of reflected particles significantly depends on the structure of the regolith. Our simulations predict that 85% of the volume in the regolith is made up of empty space between grains. These results thus show how measurements of reflected particles can be applied for studying soil properties of the Moon, as well as other planetary bodies such as Mercury.

1. Introduction

The surfaces of airless bodies are covered by a porous regolith, a loose ensemble of rocks and dust grains, due to a multitude of erosion and impact processes over billions of years (McKay et al., 1991). Its upper layers determine how those planetary bodies are observed as their surface morphology strongly affects optical properties (Hapke, 2008; Vernazza et al., 2012). The porous structure of stacked grains will also influence the interaction of any planet, moon, or asteroid with its environment or precipitating radiation. Especially the effect of porosity on thermal conductivity has been of recent interest (Ryan et al., 2022; Wood, 2020). The porosity of the upper regolith is also connected to the mechanical properties of the grain stacking (Kiuchi & Nakamura, 2014) as well as grain transport processes across a planetary surface (Schwan et al., 2017; Vernazza et al., 2012). While a large number of studies of lunar regolith have been performed, the porosity of the pristine upper regolith, defined as the ratio of voids to the total volume in the region near the surface that is accessible for precipitating radiation, is difficult to deduce from returned samples and requires non-invasive methods (Ohtake et al., 2010). Early investigations estimated a porosity value between 0.8 and 0.9 from reflectance measurements (Hapke & van Horn, 1963). Similarly, Ohtake et al. (2010) found a high porosity for the Apollo 16 sample site, which was confirmed by Hapke and Sato (2016), determining a porosity of 0.83 ± 0.03 for the upper lunar regolith at this specific site. This value for the upper regolith differs from the result of studies with returned samples of 0.52 ± 0.02 for the upper 15 cm of the lunar soil (Carrier III et al., 1991). Impacting particles, such as photons, ions, or electrons, however, have much smaller interaction regions on the order of millimeters (Hapke & Sato, 2016). It is thus questionable how applicable measurements of the porosity from returned samples are

Writing – review & editing: P. S. Szabo, A. R. Poppe, H. Biber, A. Mutzke, J. Pichler, N. Jäggi, A. Galli, P. Wurz, F. Aumayr

for the upper regolith. Specifically investigating the top layers of returned samples is not feasible either, as the original grain order is disturbed in the sample collection process.

A major external influence that affects airless bodies is the precipitation of ions from the solar wind. Their interaction with planetary surfaces is of great interest for space weathering studies as ion impacts can contribute to nanophase Fe formation, the creation of amorphized rims, or hydroxyl formation by proton implantation (Hapke, 2001; Jones et al., 2018; Keller et al., 2021; Pieters & Noble, 2016; Poppe et al., 2018). Understanding ion impacts on regolith grains is also key for determining the particle environment around airless bodies: Atoms sputtered from the surface significantly contribute to exospheres around larger bodies like Mercury (Pfleger et al., 2015) or the Moon (Wurz et al., 2007, 2022). The sputtering by ion impacts is very much dependent on the structure of the surface on a microscopic scale (Cassidy & Johnson, 2005; Küstner et al., 1998). Solar wind ions can also be scattered off the surface, which has been studied in detail for the interaction between the Moon and solar wind protons. Energetic neutral atom (ENA) measurements from the Earth-orbiting IBEX mission (McComas et al., 2009) and the Chandrayaan-1 lunar orbiter (Wieser et al., 2009) determined between 10% and 20% of solar wind protons are reflected as neutrals. Recently, the Chang'E-5 lander also reported the first measurements of ENA emission obtained from the lunar surface (Zhang et al., 2020). KAGUYA and ARTEMIS analyses have further shown that up to about 1% of protons are scattered from the lunar surface as ions (Lue et al., 2018; Saito et al., 2008). Both populations have since been characterized extensively and show several features that are not yet understood but may be related to regolith properties. For example, an incidence-angle-independent reflection coefficient (Vorburger et al., 2013), a preferential backward emission toward the impact direction (Lue et al., 2018; Schaufelberger et al., 2011), and a significantly reduced reflection energy (Futaana et al., 2012) have been reported. All these effects are also expected to occur on Mercury (Lue et al., 2017), which will be investigated by the upcoming BepiColombo mission (Orsini et al., 2021).

The investigation of reflected solar wind protons is an important part of understanding how the surfaces of airless bodies are affected by precipitating ions. In this context, the exact interaction will strongly be influenced by the properties of the bodies' regolith. Here we present simulations of the scattering of solar wind protons from lunar regolith with the program SDTrimSP-3D. Using this model, we compare the reflection coefficients to measurements from Chandrayaan-1 for ENA emission from the surface of the Moon. We find that the reflection coefficient is highly dependent on the porosity of the regolith. Our simulations lead to a precise agreement with spacecraft measurements for a highly porous, fairy-castle-like regolith structure. Following these findings, we propose the possibility of ENA emission measurements as a non-invasive method for studying the porosity of the regolith of airless bodies. This method would be feasible from orbit, especially if solar wind parameters and surface mineralogy can be constrained from accompanying measurements.

2. Simulation Methods

2.1. SDTrimSP-3D

Simulations of the solar wind proton interaction with lunar regolith were performed with SDTrimSP-3D (versions 1.15 and 1.17) (Von Toussaint et al., 2017). This software allows the simulation of ion impacts on a solid based on the Binary Collision Approximation (BCA). Within the BCA, the paths of ions and any newly created recoil atoms are traced through the solid sequentially. Scattering angles and energy losses are calculated from binary collisions with target atoms based on a given screened Coulomb interatomic potential. BCA codes such as TRIM (Biersack & Haggmark, 1980; Ziegler et al., 2010) or SDTrimSP (Mutzke et al., 2019) represent commonly used tools for calculating ion ranges, ion-induced damage formation, sputtering, and ion reflection. SDTrimSP-3D represents a three-dimensional expansion of SDTrimSP and allows the implementation of a surface morphology or more complex structures on a grid of cuboid voxels. SDTrimSP is often used for studying ion-surface interaction in nuclear fusion research (Oberkofler et al., 2015; Schmitz et al., 2018; Sugiyama et al., 2016), and has also been applied for simulating systems relevant to space weathering to better understand sputtering (Morrissey et al., 2022; Schaible et al., 2017; Szabo, Biber, Jäggi, Brenner, et al., 2020; Szabo, Biber, Jäggi, Wappl, et al., 2020), ion implantation (Biber et al., 2020), or ion-induced surface composition changes (Christoph et al., 2022). The scattering of ions from surfaces has also been compared to SDTrimSP simulations by Deuzeman (2019), finding a good agreement with experimental data for several cases. SDTrimSP-3D applications have mostly focused on sputter simulations of rough surfaces (Arredondo et al., 2019; Kelemen et al., 2021;

Von Toussaint et al., 2017), as well as the change of the surface topography as a result of prolonged ion bombardment (Arredondo et al., 2020).

2.2. Simulating Impacts of Solar Wind Protons on the Lunar Surface

In the present study, we apply SDTrimSP-3D to simulate the scattering of impinging solar wind protons from lunar regolith. Due to the approach of following the whole path of a particle in the BCA simulation, effects such as local incidence angles, impacts on multiple grains due to reflection, or implantation are automatically included. All simulations presented here were performed in the static mode of SDTrimSP-3D, where changes in the grain morphology or in the relative surface concentration of various elements are not considered.

SDTrimSP-3D requires several inputs regarding parameters for the target material and the scattering events. For the presented simulations, we use a regolith fully consisting of enstatite grains ($MgSiO_3$) with a base density of 3.3 g/cm^3 as an analog mineral for the lunar surface (Jäggi et al., 2021). The simulation-specific input parameters were adopted from sputter simulations of several silicates that achieved a precise agreement with experimental results (see e.g., Biber et al., 2020; Szabo, Biber, Jäggi, Brenner, et al., 2020; Szabo, Biber, Jäggi, Wappl, et al., 2020). Specifically, this includes a Krypton-Carbon (KrC) interaction potential (SDTrimSP-3D input parameter ipot = 1, see the example 'tri.inp' input file included in the accompanying dataset to this manuscript (Szabo, Poppe, et al., 2022)), a Gauss–Legendre integration (iintegral = 2) and electronic stopping from an average of the Lindhard-Scharff and the Oen-Robinson model (inel0 = 3). For the surface binding energies, adapted values fitted to experiments were used (Szabo, Biber, Jäggi, Brenner, et al., 2020), but these inputs only affect sputtering and are not important for simulating the reflection of impinging ions.

2.3. Implementing a Regolith Model in SDTrimSP-3D

For the implementation of a regolith surface in SDTrimSP-3D, a setup of stacked grains of equal size (diameter d_g) was chosen. In general, modeling regolith as an ensemble of spherical grains represents a commonly applied approach (see e.g., Jiang et al. (2013); Schräpler et al. (2015) and references therein). In order to implement such a grain setup, we used an algorithm of dropping spheres into a box with periodic boundary conditions (see e.g., Ryan et al., 2022). Spheres that hit the lower boundary surface of the box become frozen in place and spheres colliding with other frozen spheres have a probability to stick and also becoming frozen. This sticking probability affects the porosity of the final grain structure (see Kulchitsky et al., 2018). Using this approach, randomly stacked grain setups with porosities between about 0.5 and 0.9 can be achieved. The porosity is here calculated as the fraction of space between the grains and the total volume between the lower boundary of the simulation cell and the top of the uppermost grain.

Using this setup of stacked spheres as a base, we then create an input file for SDTrimSP-3D. For this purpose, the case_geo = 45 setting of SDTrimSP-3D is used, which allows to set up of a "fig.inp" input file that includes the coordinates of every single voxel. We transfer the grain stacking results from the sphere-dropping algorithm to this file, taking into account the chosen size and resolution of the simulation cell. Details of the optimization of the grain sizes and simulation resolution are given in the Supporting Information. At mean grain sizes of several tens of μm (McKay et al., 1991) and ion ranges of tens of nm, the ion impacts are localized to the very surface of the grain and their finite size does not affect the interaction (Nietiadi et al., 2014). However, smaller grain sizes - which indeed still uphold the requirement of local interaction near the surface - were used for computational reasons.

Analysis of returned lunar samples has clearly shown that regolith grains are not spherical, but occur in highly variable irregular shapes (Carrier III et al., 1991; McKay et al., 1991). For this reason, we did not only consider spherical grains in the SDTrimSP-3D simulations but also irregularly shaped grains. We implemented different grain shapes with a given fractal dimension f_d as a roughness characterization parameter, following an algorithm proposed by Wei et al. (2018) for creating random irregularly shaped particles. The fractal dimension f_d describes how the surface area changes with measurement scale: A smooth sphere has $f_d = 2$, while f_d increases for rougher surfaces to a maximum value of 3. The algorithm by Wei et al. (2018) then connects f_d to an expansion of the grain shape in spherical harmonics $Y_n^m(\theta, \varphi)$ for polar angles θ and azimuthal angles φ. We used this algorithm to create random irregular grain shapes, using the inputs from Wei et al. (2018) for highly decomposed granite and accounting for fractal dimensions between 2.2 and 2.8 to cover a broad range of possible shapes (see the Support-

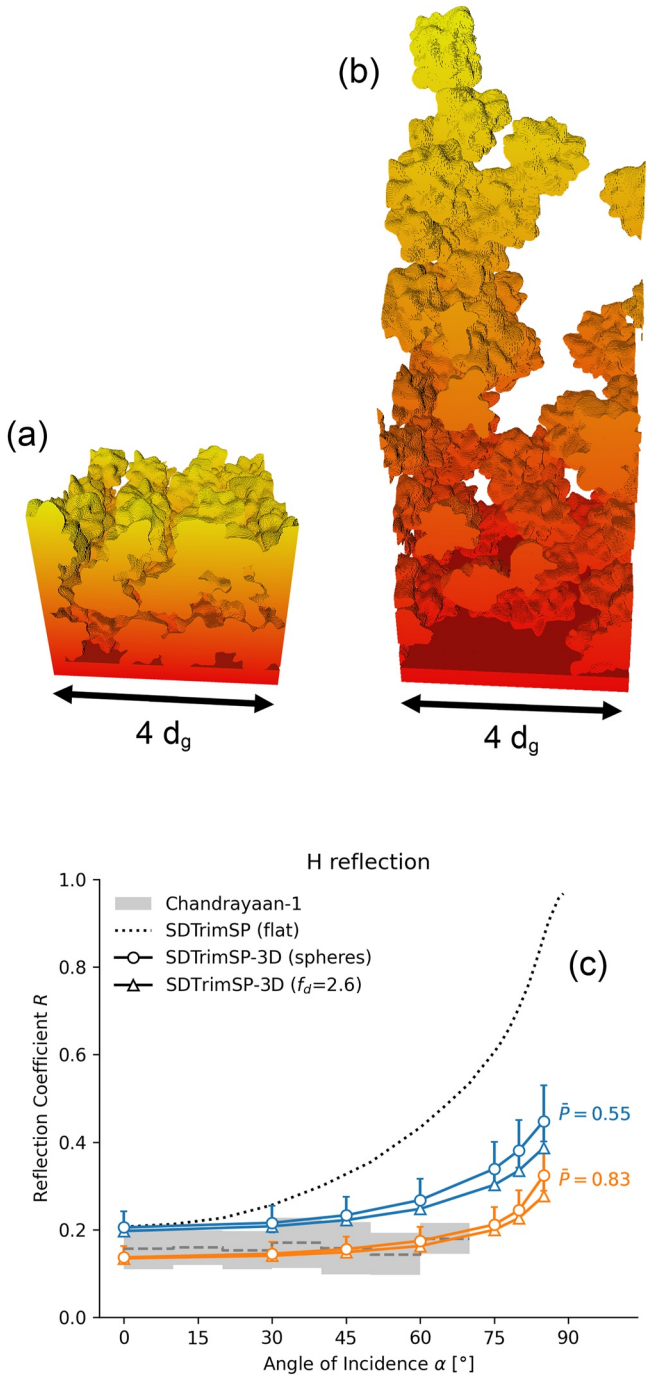

Figure 1. (a) An example of a regolith setup with a porosity of about 0.5 and a grain fractal dimension $f_d = 2.6$. (b) In the same manner, as in (a), a regolith setup with a porosity of about 0.8 is depicted. (c) The reflection coefficient R for different angles of incidence α is shown. Chandrayaan-1 measurements (Vorburger et al., 2013) are compared to simulations with a flat surface (dotted line), spherical grains (circles) and irregularly shaped grains with $f_d = 2.6$ (triangles). Agreement between simulations and experiments is much better for the very porous regolith (mean porosity $\bar{P} = 0.83$, orange) than for the tighter packing with lower porosity ($\bar{P} = 0.55$, blue).

ing Information). For the fractal dimension of lunar regolith grains, only a limited number of studies are available. Shkuratov and Helfenstein (2001) derived a high fractal dimension of the lunar regolith structure on the microscopic scale of 2.7 from measurements of scattered light from the Moon. Tianxiang et al. (2015) analyzed the shapes of lunar regolith analogs and report fractal dimensions between 2.44 and 2.88, supporting that high values of f_d can be expected for regolith grains.

Figure 1 shows examples of the final regolith setups in SDTrimSP-3D for grains with $f_d = 2.6$ and a porosity of about 0.5 (Figures 1a) and 0.8 (Figure 1b). For the irregularly shaped grains, only grains with the same f_d were used, but each grain was randomly generated independently from the others. The grains on the edge of the simulation cell appear cut off because of the periodic boundary conditions of the simulation cell. For the regolith setups, 50 grains were used to ensure that the regolith is extended enough that ions do not pass through the regolith into the solid base below the stacked grains. Test runs were performed with 100 spherical grains in the same cell for several cases, which gave results consistent with simulations containing 50 grains. All simulation cells had a base 4 $d_g \times 4$ d_g with grain diameter d_g, typical regolith heights that resulted from the grain dropping algorithm were about 3 d_g for the lower porosity and about 9 d_g for the high porosity setups.

3. Results

Using the regolith setups with variable porosity and different grain shapes described in the previous section, we performed simulations of the reflection of solar wind protons to compare them to measurements of ENA emission from the surface of the Moon. For this purpose, we chose the data from the Chandrayaan-1 Energetic Neutrals Analyzer (CENA) (Vorburger et al., 2013), where an overall neutral reflection coefficient R of 0.16 ± 0.05 was found with no significant dependence on the angle of incidence. Using data from the whole CENA operation time between January 2009 and July 2009, we took this evaluation as being the most representative of the global reflection of solar wind protons from the lunar surface. In order to have a suitable reference for the solar wind conditions during the timespan of the CENA measurements, we used the OMNI dataset (King & Papitashvili, 2005) to derive the solar wind energy distribution as input for SDTrimSP-3D. As similarly described by Schaufelberger et al. (2011), we find solar wind energies between about 350 and 1,700 eV with a peak at 500 eV and a mean energy of about 750 eV (see Supporting Information).

SDTrimSP-3D cannot treat the neutralization process of precipitating protons. Instead, only the total reflection of all solar wind protons independent of the incident charge state can be calculated. Lue et al. (2018) showed that the solar wind proton scattering efficiency as a charged particle is between 0.2% and 0.6%. Thus, ENAs are estimated to make up between about 96% and 99% of the reflected particles. We therefore directly compare SDTrimSP-3D results to ENA measurements and consider the charged particle emission probability as one of the possible sources of uncertainty.

3.1. Reflection Coefficients for Different Porosity Regimes

Figure 1c compares simulation results of the reflection coefficient R for ions with the solar wind energy distribution from the OMNI dataset to the CENA measurements from Vorburger et al. (2013) (gray area) under differ-

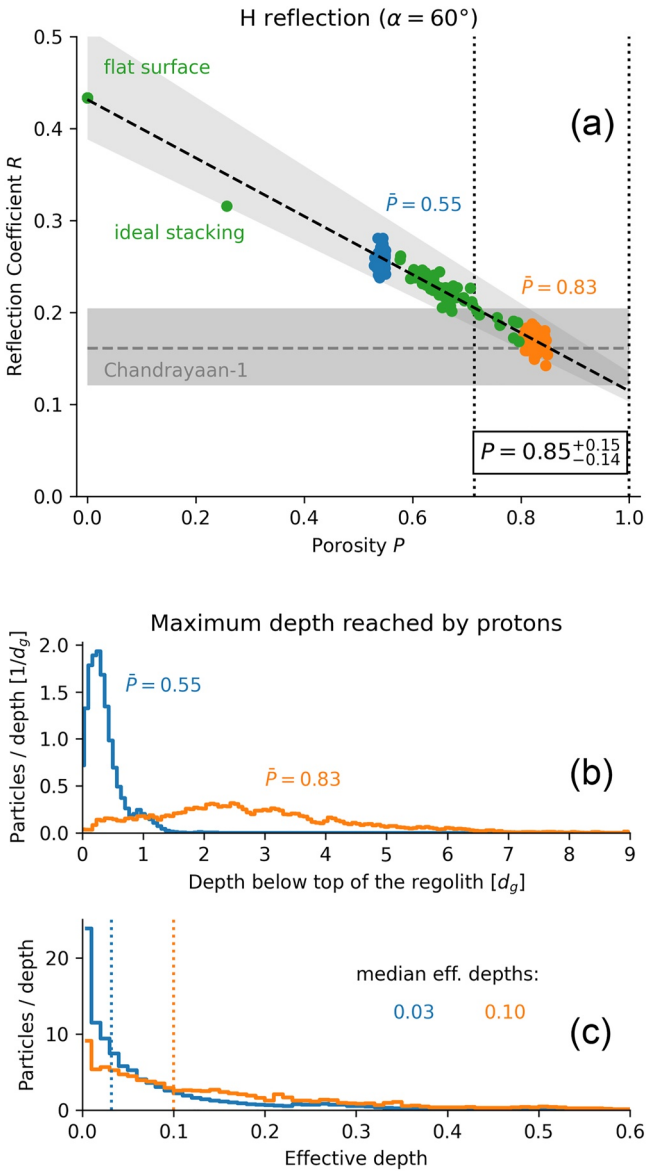

Figure 2. (a) For an angle of incidence α of 60°, simulated reflection coefficients R are plotted over the porosity P. The same data as in Figure 1c are shown in blue and orange, while green data points represent simulations from a flat surface, an ideal hexagonal packing, and a set of random porosities between 0.55 and 0.8. Comparing the linear fit for the simulation results (black dashed line) to the Chandrayaan-1 measurements gives a porosity value of $P = 0.85^{+0.15}_{-0.14}$ for the lunar surface. (b) For simulations with porosities of 0.55 (blue) and 0.83 (orange), the maximum depth below the top of the regolith reached by impacting protons (in units of grain diameter d_g) is plotted. (c) To eliminate the role of the different total volumes taken up by the regolith, the frequency of maximum proton depths is plotted over the effective depth, that is, the fraction of the total regolith grain volume that is above the point of reference. For lower porosities, still more impacts happen at lower effective depths, where reflection and escape from the regolith structure are more likely.

ent incidence angles with respect to the surface normal. Simulations with a flat surface (black dotted line, simulated with the graphical user interface for SDTrimSP from Szabo, Weichselbaum, et al. (2022) describe a vastly different scenario than the CENA measurements. While the reflection coefficients from the lunar surface show no dependence on the incidence angle (at least up to the measurement limit of 70°), a pronounced increase in the reflection coefficient is predicted for a flat surface under oblique incidence. In contrast, the SDTrimSP-3D regolith simulations show a much flatter behavior and the simulations with a high porosity (orange) agree very well with the CENA data. With a mean porosity $\bar{P} = 0.83$, these regolith structures correspond to the porosity result from Hapke and Sato (2016) and closely resemble the example in Figure 1b. Simulations using a more efficient packing with lower porosity (blue) overestimate the CENA measurements, especially for higher incidence angles. Their mean porosity $\bar{P} = 0.55$ leads to structures similar to the example in Figures 1a and is closer to data from returned lunar samples (Carrier III et al., 1991). The SDTrimSP-3D results shown in Figure 1c include calculations with spherical grains (circular symbols) as well as with irregular grains with $f_d = 2.6$ (triangular symbols). However, the grain shape only starts to affect the simulation results for incidence angles over 60°. Similar behavior is found for other f_d values of 2.2, 2.4, 2.7, and 2.8 (see the Supporting Information).

The error bars in Figure 1c give an uncertainty estimate for the SDTrimSP-3D simulation of [−10%, +18%] based on uncertainties from the choice of grain size, voxel size, mineralogy, electronic stopping model and the fact that a small fraction of solar wind protons (between 0.2% and 0.6%) is reflected as charged particles instead of as neutrals (Lue et al., 2018). For the mineral-related estimate, we simulated reflection coefficients from anorthite, forsterite, and the average lunar composition from Wurz et al. (2007), which lie within 5% of the enstatite result. The asymmetry in the uncertainty estimate originates from general inaccuracies for the stopping of oxides that were discussed by Roth et al. (2017). There it was found that the commonly applied weighted average of elemental stopping powers for calculating the compound stopping power significantly overestimates measured values for several oxides. For the relevant proton energies in our simulations, the SiO_2 stopping power is about 30%–35% smaller (Roth et al., 2017). A correction by 30% would result in an increase of the reflection coefficient for enstatite by 16.5% as predicted by SDTrimSP-3D. Due to unclear differences in the stopping between SiO_2 and $MgSiO_3$, we include this as a potential source of uncertainty.

In comparison to the Chandrayaan-1 data, the difference between low porosity and high porosity still remains evident when uncertainties are considered. A tightly packed regolith cannot explain the measured ENA reflection coefficients. Instead, the agreement for all angles is only achieved when a very porous, fairy-castle-like structure is assumed in the simulation.

3.2. Determining Porosity From Reflection Coefficients

The data presented in Figure 1c show that the reflection coefficient of solar wind protons changes with different regolith porosities. As seen in Figure 1c, the porosity dependence at 60° incidence is more pronounced than at lower incidence angles, but at the same time, the simulation results still show no signs of significant grain shape influences. Figure 2a then depicts the dependence of the reflection coefficient on the porosity P for a fixed angle of incidence of 60°. The incidence angle of 60° is thus well suited to constrain the porosity of the upper lunar regolith.

The data from Figure 1c for low and high porosities and all grain shapes are included in blue and orange, while additional simulations are shown in green. This includes the SDTrimSP result for a flat surface (with a porosity of 0), an ideal hexagonal close packing of spheres with a porosity of 0.26, as well as several SDTrimSP-3D simulations with spherical grains and random porosities between 0.55 and 0.8. For porosities above 0.5, a linear fit of $R = 0.432 - 0.317 \times P$ was calculated for the simulation results (black dashed line). As discussed before, uncertainties of the calculated reflection coefficients have to be taken into account as well (light-gray-shaded area around the linear fit), which we assume to scale the same for all simulations regardless of porosity or grain shape. From the comparison of the fit to SDTrimSP-3D results and the Chandrayaan-1 measurement for 60° (gray, from Vorburger et al. [2013]), a porosity of the upper lunar regolith of $P = 0.85^{+0.15}_{-0.14}$ can be derived.

4. Discussion

SDTrimSP-3D simulations of the reflection of solar wind protons from the lunar regolith allow essential insights into the interaction of the solar wind with the surface of airless bodies. Our simulation results provide a precise quantitative agreement with the ENA measurements from the CENA instrument on Chandrayaan-1 in both the absolute value of the reflection coefficient and its lack of a significant angular dependence for incidence angles less than about 60°. The observed behavior is similar to generally reported changes in the sputter yield with increased surface roughness (Cupak et al., 2021; Szabo, Cupak, et al., 2022). This underlines the importance of taking the regolith structure into account, in particular, the top-most layer with the highest porosity, to understand how airless bodies are affected by impacting ions. It also supports the validity of using our SDTrimSP-3D approach to model ion-surface interactions on airless bodies. Given similar behaviors for granular structures and rough surfaces, investigating the possibility of approximating the regolith as a conventional rough surface in a future study could provide a promising way of easier modeling the ion interaction with regolith.

Grain shapes only have minor effects on the simulation results, as similarly reported by Cassidy and Johnson (2005). However, solar wind proton reflection is significantly dependent on the porosity of the uppermost regolith layers, where ions as well as other precipitating radiation impact the surface. This result stands in contrast to the calculations by Cassidy and Johnson (2005), where no porosity dependence was found. However, Cassidy and Johnson (2005) assumed isotropic, random distances between atom collisions with grains, which differs from our geometry of stacked regolith grains. For such structures, increasing porosity will lead to fewer precipitating ions impacting grains at the top of the structure, where reflected particles have a large free solid angle for escaping. This is visualized in Figures 2b and 2c: Figure 2b shows the maximum depth that impacting protons reach from multiple simulations with mean porosities of 0.55 (blue) and 0.83 (orange), respectively. For the lower porosity, this depth is much smaller than for the fairy-castle like structure, which is evident from the influence of the stacking on the total height of the simulation cell (see Figure 1). To compensate for this, we define an *effective* depth between 0 and 1 as the fraction of the volume of all regolith grains above the given depth. Figure 2c then shows that regions near the top of the regolith are still much easier access for the lower porosity case due to the tighter packing at the very top of the regolith. This is also underlined by the median effective depth of 0.03 for $\bar{P} = 0.55$ and 0.10 for $\bar{P} = 0.83$. From the top of any regolith structure, reflection and escape are easier and this contribution is missing for the higher porosity structures. Instead, particles reaching deeper into the regolith become more prominent for loosely stacked regolith. After local scattering at a grain, these particles then have an increased probability to hit another grain and become implanted there, contributing to an overall decreased reflection of incident protons. This more effective trapping of incident protons can also be seen in the median of the number of collisions reflected protons undergo, which is about 10% higher for the high porosity case than for the regolith structures with porosities of around 0.55.

Our calculated porosity of the lunar surface of $P = 0.85^{+0.15}_{-0.14}$ is in line with the value of 0.83 ± 0.03 found from infrared reflectance measurements (Hapke & Sato, 2016). However, the result of Hapke and Sato (2016) is - strictly speaking - only valid for the Apollo 16 landing site, while the ENA measurements allow the determination of the porosity of the upper lunar regolith on a global scale. Figure 2b shows the depth that solar wind protons can access in the regolith. With mean grain diameters of the lunar soil between about 60 and 80 μm (McKay et al., 1991), this corresponds to several 100 μm on the Moon. The porosity value derived from ENA emission is thus valid for the same depth range. Existing uncertainties in the porosity from SDTrimSP-3D simulations are mostly connected to measurement uncertainties in the ENA reflection coefficient from Chandrayaan-1 and some

lack of constraints for SDTrimSP-3D input parameters. Simulation uncertainties can be improved by future calibration of SDTrimSP-3D simulations with laboratory measurements of the reflection of protons from lunar soil, which would directly enhance the precision of ENA measurements for determining porosity. Most importantly, the reflection coefficient was also found to only have a minor dependence on most lunar minerals and is thus not sensitive to an exact knowledge of element abundances of a planetary surface. This represents a contrast to infrared reflectance, which can be affected by a wide range of surface properties. Characterization of the porosity of the Apollo 16 sampling site to the described extent was only possible due to the comparison of orbital data with laboratory measurements of returned samples (Hapke, 2001). In contrast, ENA measurements are fully feasible from an orbiting spacecraft. The energy of precipitating protons plays a bigger role in ion impacts, but measuring the ENA reflection coefficient is not possible without characterizing the solar wind anyway. Therefore, any orbiter that is equipped with instruments to measure solar wind (or other ambient plasma) parameters and ENA emission could be able to study the regolith porosity on an airless body, given some constraints on the major minerals present on the surface.

One obvious example, where such studies will be of use, is the upcoming BepiColombo mission to Mercury. It recently completed its first two Mercury flybys and will enter an orbit around the planet in 2025 (Mangano et al., 2021). BepiColombo is not equipped with a lander and is thus reliant on remote observations to study Mercury's surface. Besides characterization of Mercury's exosphere, ENA measurements are one of the key science goals of BepiColombo's SERENA and MPPE instruments (Orsini et al., 2021; Saito et al., 2021). These prerequisites make it ideal for using ENA measurements to constrain the porosity of the Hermean regolith. At Mercury, previous studies have either suggested a similar or a lower porosity than for the surface of the Moon (Domingue et al., 2010; Warell, 2004). The analysis of reflected solar wind protons from BepiColombo will allow additional insights into the porosity of Mercury's regolith. Its ENA instruments should thus be pointed at Mercury's surface in regular intervals to map the entire surface in reflected ENAs and take into account different solar wind conditions. These investigations would also show how the regolith structure is affected by different electrostatic dust transport or a higher micrometeoroid flux as both the exposure to solar radiation as well as the micrometeoroid environment are more intense on Mercury than on the Moon (Pokornỳ et al., 2018, 2019; Sternovsky et al., 2008).

Furthermore, the scattering of protons from the surface of Phobos has recently been studied (Futaana et al., 2010, 2021). The Martian Moons eXploration (MMX) mission will significantly add to observations of scattered ions (Yokota et al., 2021), but it is not equipped with an instrument for ENA measurements. The quantification of the total amount of reflected solar wind protons from the surface of Phobos will therefore not be possible in the same manner as it has been achieved for the Moon. However, future research on solar wind proton reflection characteristics will show if methods for deriving the porosity from protons reflected as charged particles can be established as well. This would enable studying this parameter for the surface of Phobos and other airless bodies without the need of quantifying the total reflection of solar wind protons.

5. Conclusions

We have presented 3D ion-surface interaction simulations with a regolith grain setup to calculate the reflection coefficients of solar wind protons from the lunar surface. The simulation results show that the reflection from the regolith does not depend strongly on the angle of incidence of the precipitating ions. However, we find that the porosity of the regolith structure is an important parameter for the proton reflection process, while the grain shapes within our tested parameter set only affect the outcome for very oblique impacts. For an incidence angle of 60° in reference to the surface normal, we deduce a linear dependence of the reflection coefficient R on the porosity P. A comparison of SDTrimSP-3D simulation results to ENA emission measurements from Chandrayaan-1 shows that the spacecraft measurements are best explained by a very porous, fairy castle regolith structure. For the upper lunar regolith, a high porosity of $P = 0.85^{+0.15}_{-0.14}$ can be calculated, representing an average for the whole surface of the Moon. This supports significant adhesion between lunar regolith grains and could also indicate that electrostatic dust transport of single grains plays an important role in forming the uppermost regolith layers (Hood et al., 2022; Schwan et al., 2017; Wang et al., 2016; Yeo et al., 2021). These results are in agreement with previous infrared measurements of the Apollo 16 landing site (Hapke & Sato, 2016). Compared to such infrared studies, ENA reflection coefficients are less sensitive to other surface parameters and thus less dependent on laboratory calibration. Therefore, we propose ENA measurements as a feasible method of characterizing the

regolith porosity of an airless body with an orbiting spacecraft. It will already be possible to apply this method for the Hermean regolith, as both modules of the BepiColombo spacecraft will analyze ENA emission from the surface of Mercury.

Data Availability Statement

The research data presented in this manuscript is included in the accompanying dataset uploaded on Figshare and can be accessed at https://doi.org/10.6084/m9.figshare.20511039.v1 (Szabo, Poppe, et al., 2022).

Acknowledgments
The authors gratefully acknowledge support from NASA's Solar System Research Virtual Institute (SSERVI) via the LEADER team, Grant #80NSSC20M0060. Financial support has also been provided by the Austrian Science Fund FWF (Project No. I 4101-N36) and by the Swiss National Science Foundation (SNSF) (Fund 200021L182771/1).

References

Arredondo, R., Balden, M., Mutzke, A., Von Toussaint, U., Elgeti, S., Höschen, T., et al. (2020). Impact of surface enrichment and morphology on sputtering of EUROFER by deuterium. *Nuclear Materials and Energy*, *23*, 100749. https://doi.org/10.1016/j.nme.2020.100749

Arredondo, R., Oberkofler, M., Schwarz-Selinger, T., von Toussaint, U., Burwitz, V., Mutzke, A., et al. (2019). Angle-dependent sputter yield measurements of keV D ions on W and Fe and comparison with SDTrimSP and SDTrimSP-3D. *Nuclear Materials and Energy*, *18*, 72–76. https://doi.org/10.1016/j.nme.2018.12.007

Biber, H., Szabo, P. S., Jäggi, N., Wallner, M., Stadlmayr, R., Moro, M. V., et al. (2020). Solar wind Helium ion interaction with Mg and Fe rich pyroxene as Mercury surface analogue. *Nuclear Instruments and Methods in Physics Research Section B: Beam Interactions with Materials and Atoms*, *480*, 10–15. https://doi.org/10.1016/j.nimb.2020.07.021

Biersack, J. P., & Haggmark, L. G. (1980). A Monte Carlo computer program for the transport of energetic ions in amorphous targets. *Nuclear Instruments and Methods*, *174*(1–2), 257–269. https://doi.org/10.1016/0029-554x(80)90440-1

Carrier, W. D., III, Olhoeft, G. R., & Mendell, W. (1991). Physical properties of the lunar surface. *Lunar sourcebook*, 475–594.

Cassidy, T., & Johnson, R. (2005). Monte Carlo model of sputtering and other ejection processes within a regolith. *Icarus*, *176*(2), 499–507. https://doi.org/10.1016/j.icarus.2005.02.013

Christoph, J., Minesinger, G., Bu, C., Dukes, C., & Elkins-Tanton, L. (2022). Space weathering effects in troilite by simulated solar-wind hydrogen and helium ion irradiation. *Journal of Geophysical Research: Planets*, *127*(5), e2021JE006916. https://doi.org/10.1029/2021JE006916

Cupak, C., Szabo, P. S., Biber, H., Stadlmayr, R., Grave, C., Fellinger, M., et al. (2021). Sputter yields of rough surfaces: Importance of the mean surface inclination angle from nano-to microscopic rough regimes. *Applied Surface Science*, *570*, 151204. https://doi.org/10.1016/j.apsusc.2021.151204

Deuzeman, M. J. (2019). *Generation and interactions of energetic tin ions (Unpublished doctoral dissertation)*. Rijksuniversiteit Groningen.

Domingue, D. L., Vilas, F., Holsclaw, G. M., Warell, J., Izenberg, N. R., Murchie, S. L., et al. (2010). Whole-disk spectrophotometric properties of Mercury: Synthesis of MESSENGER and ground-based observations. *Icarus*, *209*(1), 101–124. https://doi.org/10.1016/j.icarus.2010.02.022

Futaana, Y., Barabash, S., Holmström, M., Fedorov, A., Nilsson, H., Lundin, R., et al. (2010). Backscattered solar wind protons by Phobos. *Journal of Geophysical Research*, *115*(A10). https://doi.org/10.1029/2010ja015486

Futaana, Y., Barabash, S., Wieser, M., Holmström, M., Lue, C., Wurz, P., et al. (2012). Empirical energy spectra of neutralized solar wind protons from the lunar regolith. *Journal of Geophysical Research*, *117*(E5). https://doi.org/10.1029/2011je004019

Futaana, Y., Holmström, M., Fedorov, A., & Barabash, S. (2021). Does phobos reflect solar wind protons? Mars Express special flyby operations with and without the presence of phobos. *Journal of Geophysical Research: Planets*, *126*(11), e2021JE006969. https://doi.org/10.1029/2021je006969

Hapke, B. (2001). Space weathering from Mercury to the asteroid belt. *Journal of Geophysical Research*, *106*(E5), 10039–10073. https://doi.org/10.1029/2000je001338

Hapke, B. (2008). Bidirectional reflectance spectroscopy: 6. Effects of porosity. *Icarus*, *195*(2), 918–926. https://doi.org/10.1016/j.icarus.2008.01.003

Hapke, B., & Sato, H. (2016). The porosity of the upper lunar regolith. *Icarus*, *273*, 75–83. https://doi.org/10.1016/j.icarus.2015.10.031

Hapke, B., & van Horn, H. (1963). Photometric studies of complex surfaces, with applications to the Moon. *Journal of Geophysical Research*, *68*(15), 4545–4570. https://doi.org/10.1029/jz068i015p04545

Hood, N., Carroll, A., Wang, X., & Horányi, M. (2022). Laboratory measurements of size distribution of electrostatically lofted dust. *Icarus*, *371*, 114684. https://doi.org/10.1016/j.icarus.2021.114684

Jäggi, N., Galli, A., Wurz, P., Biber, H., Szabo, P. S., Brötzner, J., et al. (2021). Creation of Lunar and Hermean analogue mineral powder samples for solar wind irradiation experiments and mid-infrared spectra analysis. *Icarus*. https://doi.org/10.1016/j.icarus.2021.114492

Jiang, M., Shen, Z., & Thornton, C. (2013). Microscopic contact model of lunar regolith for high efficiency discrete element analyses. *Computers and Geotechnics*, *54*, 104–116. https://doi.org/10.1016/j.compgeo.2013.07.006

Jones, B. M., Aleksandrov, A., Hibbitts, K., Dyar, M., & Orlando, T. M. (2018). Solar wind-induced water cycle on the Moon. *Geophysical Research Letters*, *45*(20), 10–959. https://doi.org/10.1029/2018gl080008

Kelemen, M., Schwarz-Selinger, T., Mutzke, A., Balden, M., Vassallo, E., Pedroni, M., et al. (2021). Influence of surface roughness on the sputter yield of Mo under keV D ion irradiation. *Journal of Nuclear Materials*, *555*, 153135. https://doi.org/10.1016/j.jnucmat.2021.153135

Keller, L. P., Berger, E. L., Zhang, S., & Christoffersen, R. (2021). Solar energetic particle tracks in lunar samples: A transmission electron microscope calibration and implications for lunar space weathering. *Meteoritics & Planetary Science*, *56*(9), 1685–1707. https://doi.org/10.1111/maps.13732

King, J., & Papitashvili, N. (2005). Solar wind spatial scales in and comparisons of hourly Wind and ACE plasma and magnetic field data. *Journal of Geophysical Research*, *110*(A2). https://doi.org/10.1029/2004ja010649

Kiuchi, M., & Nakamura, A. M. (2014). Relationship between regolith particle size and porosity on small bodies. *Icarus*, *239*, 291–293. https://doi.org/10.1016/j.icarus.2014.05.029

Kulchitsky, A. V., Hurley, D. M., Johnson, J. B., Duvoy, P. X., & Zimmerman, M. (2018). Solar wind access to grains in the upper layer of regolith. *Journal of Geophysical Research: Planets*, *123*(4), 972–981. https://doi.org/10.1002/2017je005392

Küstner, M., Eckstein, W., Dose, V., & Roth, J. (1998). The influence of surface roughness on the angular dependence of the sputter yield. *Nuclear Instruments and Methods in Physics Research Section B: Beam Interactions with Materials and Atoms*, *145*(3), 320–331. https://doi.org/10.1016/s0168-583x(98)00399-1

Lue, C., Futaana, Y., Barabash, S., Wieser, M., Bhardwaj, A., Wurz, P., & Asamura, K. (2017). Solar wind scattering from the surface of Mercury: Lessons from the moon. *Icarus*, *296*, 39–48. https://doi.org/10.1016/j.icarus.2017.05.019

Lue, C., Halekas, J., Poppe, A., & McFadden, J. (2018). ARTEMIS observations of solar wind proton scattering off the lunar surface. *Journal of Geophysical Research: Space Physics*, *123*(7), 5289–5299. https://doi.org/10.1029/2018ja025486

Mangano, V., Dósa, M., Fränz, M., Milillo, A., Oliveira, J. S., Lee, Y. J., et al. (2021). BepiColombo science investigations during cruise and flybys at the Earth, Venus and Mercury. *Space Science Reviews*, *217*(1), 1–81. https://doi.org/10.1007/s11214-021-00797-9

McComas, D., Allegrini, F., Bochsler, P., Frisch, P., Funsten, H., Gruntman, M., et al. (2009). Lunar backscatter and neutralization of the solar wind: First observations of neutral atoms from the Moon. *Geophysical Research Letters*, *36*(12). https://doi.org/10.1029/2009gl038794

McKay, D. S., Heiken, G., Basu, A., Blanford, G., Simon, S., Reedy, R., et al. (1991). The lunar regolith. *Lunar Sourcebook*, *567*, 285–356.

Morrissey, L. S., Tucker, O. J., Killen, R. M., Nakhla, S., & Savin, D. W. (2022). Solar wind ion sputtering of sodium from silicates using molecular dynamics calculations of surface binding energies. *The Astrophysical Journal Letters*, *925*(1), L6. https://doi.org/10.3847/2041-8213/ac42d8

Mutzke, A., Schneider, R., Eckstein, W., Dohmen, R., Schmid, K., Toussaint, U. v., & Badelow, G. (2019). SDTrimSP version 6.00.

Nietiadi, M. L., Sandoval, L., Urbassek, H. M., & Möller, W. (2014). Sputtering of Si nanospheres. *Physical Review B*, *90*(4), 045417. https://doi.org/10.1103/physrevb.90.045417

Oberkofler, M., Alegre, D., Aumayr, F., Brezinsek, S., Dittmar, T., Dobes, K., et al. (2015). Plasma–wall interactions with nitrogen seeding in all-metal fusion devices: Formation of nitrides and ammonia. *Fusion Engineering and Design*, *98*, 1371–1374. https://doi.org/10.1016/j.fusengdes.2015.01.044

Ohtake, M., Matsunaga, T., Yokota, Y., Yamamoto, S., Ogawa, Y., Morota, T., et al. (2010). Deriving the absolute reflectance of lunar surface using SELENE (Kaguya) multiband imager data. *Space Science Reviews*, *154*(1), 57–77. https://doi.org/10.1007/978-1-4419-8122-6_3

Orsini, S., Livi, S., Lichtenegger, H., Barabash, S., Milillo, A., De Angelis, E., et al. (2021). Serena: Particle instrument suite for determining the Sun-Mercury interaction from BepiColombo. *Space Science Reviews*, *217*(1), 1–107.

Pfleger, M., Lichtenegger, H., Wurz, P., Lammer, H., Kallio, E., Alho, M., et al. (2015). 3D-modeling of Mercury's solar wind sputtered surface-exosphere environment. *Planetary and Space Science*, *115*, 90–101. https://doi.org/10.1016/j.pss.2015.04.016

Pieters, C. M., & Noble, S. K. (2016). Space weathering on airless bodies. *Journal of Geophysical Research: Planets*, *121*(10), 1865–1884. https://doi.org/10.1002/2016je005128

Pokornỳ, P., Janches, D., Sarantos, M., Szalay, J. R., Horányi, M., Nesvornỳ, D., & Kuchner, M. J. (2019). Meteoroids at the moon: Orbital properties, surface vaporization, and impact ejecta production. *Journal of Geophysical Research: Planets*, *124*(3), 752–778. https://doi.org/10.1029/2018JE005912

Pokornỳ, P., Sarantos, M., & Janches, D. (2018). A comprehensive model of the meteoroid environment around Mercury. *The Astrophysical Journal*, *863*(1), 31.

Poppe, A., Farrell, W., & Halekas, J. S. (2018). Formation timescales of amorphous rims on lunar grains derived from ARTEMIS observations. *Journal of Geophysical Research: Planets*, *123*(1), 37–46. https://doi.org/10.1002/2017je005426

Roth, D., Bruckner, B., Undeutsch, G., Paneta, V., Mardare, A., McGahan, C., et al. (2017). Electronic stopping of slow protons in oxides: Scaling properties. *Physical Review Letters*, *119*(16), 163401. https://doi.org/10.1103/physrevlett.119.163401

Ryan, A. J., Pino-Muñoz, D., Bernacki, M., Delbo, M., Sakatani, N., Biele, J., et al. (2022). Full-field modeling of heat transfer in asteroid regolith 2: Effects of porosity. *Journal of Geophysical Research: Planets*, *127*(6), e2022JE007191. https://doi.org/10.1029/2022JE007191

Saito, Y., Delcourt, D., Hirahara, M., Barabash, S., André, N., Takashima, T., et al. (2021). Pre-flight calibration and near-Earth commissioning results of the Mercury plasma particle experiment (MPPE) onboard MMO (Mio). *Space Science Reviews*, *217*(5), 1–91. https://doi.org/10.1007/s11214-021-00839-2

Saito, Y., Yokota, S., Tanaka, T., Asamura, K., Nishinos, M., Fujimoto, M., et al. (2008). Solar wind proton reflection at the lunar surface: Low energy ion measurement by MAP-PACE onboard SELENE (KAGUYA). *Geophysical Research Letters*, *35*(24). https://doi.org/10.1029/2008gl036077

Schaible, M., Dukes, C., Hutcherson, A., Lee, P., Collier, M., & Johnson, R. (2017). Solar wind sputtering rates of small bodies and ion mass spectrometry detection of secondary ions. *Journal of Geophysical Research: Planets*, *122*(10), 1968–1983. https://doi.org/10.1002/2017je005359

Schaufelberger, A., Wurz, P., Barabash, S., Wieser, M., Futaana, Y., Holmström, M., et al. (2011). Scattering function for energetic neutral hydrogen atoms off the lunar surface. *Geophysical Research Letters*, *38*(22). https://doi.org/10.1029/2011gl049362

Schmitz, J., Litnovsky, A., Klein, F., Wegener, T., Tan, X., Rasinski, M., et al. (2018). WCrY smart alloys as advanced plasma-facing materials–Exposure to steady-state pure deuterium plasmas in PSI-2. *Nuclear Materials and Energy*, *15*, 220–225. https://doi.org/10.1016/j.nme.2018.05.002

Schräpler, R., Blum, J., von Borstel, I., & Güttler, C. (2015). The stratification of regolith on celestial objects. *Icarus*, *257*, 33–46. https://doi.org/10.1016/j.icarus.2015.04.033

Schwan, J., Wang, X., Hsu, H.-W., Grün, E., & Horányi, M. (2017). The charge state of electrostatically transported dust on regolith surfaces. *Geophysical Research Letters*, *44*(7), 3059–3065. https://doi.org/10.1002/2017gl072909

Shkuratov, Y. G., & Helfenstein, P. (2001). The opposition effect and the quasi-fractal structure of regolith: I. Theory. *Icarus*, *152*(1), 96–116. https://doi.org/10.1006/icar.2001.6630

Sternovsky, Z., Chamberlin, P., Horanyi, M., Robertson, S., & Wang, X. (2008). Variability of the lunar photoelectron sheath and dust mobility due to solar activity. *Journal of Geophysical Research*, *113*(A10). https://doi.org/10.1029/2008ja013487

Sugiyama, K., Schmid, K., & Jacob, W. (2016). Sputtering of iron, chromium and tungsten by energetic deuterium ion bombardment. *Nuclear Materials and Energy*, *8*, 1–7. https://doi.org/10.1016/j.nme.2016.05.016

Szabo, P. S., Biber, H., Jäggi, N., Brenner, M., Weichselbaum, D., Niggas, A., et al. (2020). Dynamic potential sputtering of lunar analog material by solar wind ions. *The Astrophysical Journal*, *891*(1), 100. https://doi.org/10.3847/1538-4357/ab7008

Szabo, P. S., Biber, H., Jäggi, N., Wappl, M., Stadlmayr, R., Primetzhofer, D., et al. (2020). Experimental insights into space weathering of phobos: Laboratory investigation of sputtering by atomic and molecular planetary ions. *Journal of Geophysical Research: Planets*, *125*(12), e2020JE006583. https://doi.org/10.1029/2020je006583

Szabo, P. S., Cupak, C., Biber, H., Jäggi, N., Galli, A., Wurz, P., & Aumayr, F. (2022). Analytical model for the sputtering of rough surfaces. *Surfaces and Interfaces*, *30*, 101924. https://doi.org/10.1016/j.surfin.2022.101924

Szabo, P. S., Poppe, A. R., Biber, H., Mutzke, A., Pichler, J., Galli, A., et al. (2022). Deducing lunar regolith porosity from energetic neutral atom emission. [Dataset]. https://doi.org/10.6084/m9.figshare.20511039

Szabo, P. S., Weichselbaum, D., Biber, H., Cupak, C., Mutzke, A., Wilhelm, R., & Aumayr, F. (2022). Graphical user interface for SDTrimSP to simulate sputtering, ion implantation and the dynamic effects of ion irradiation. *Nuclear Instruments and Methods in Physics Research Section B: Beam Interactions with Materials and Atoms*, *522*, 47–53. https://doi.org/10.1016/j.nimb.2022.04.008

Tianxiang, D., Xuyan, H., Wanjing, P., Lixia, S., Shengyuan, J., & Qiquan, Q. (2015). Research on the shape model of particles in lunar regolith fluid based on the fractal theory. *2015 International Conference on Fluid Power and Mechatronics (FPM)*, 109–115. https://doi.org/10.1109/fpm.2015.7337095

Vernazza, P., Delbo, M., King, P., Izawa, M., Olofsson, J., Lamy, P., et al. (2012). High surface porosity as the origin of emissivity features in asteroid spectra. *Icarus*, *221*(2), 1162–1172. https://doi.org/10.1016/j.icarus.2012.04.003

Von Toussaint, U., Mutzke, A., & Manhard, A. (2017). Sputtering of rough surfaces: A 3D simulation study. *Physica Scripta*, *2017*(T170), 014056. https://doi.org/10.1088/1402-4896/aa90be

Vorburger, A., Wurz, P., Barabash, S., Wieser, M., Futaana, Y., Lue, C., et al. (2013). Energetic neutral atom imaging of the lunar surface. *Journal of Geophysical Research: Space Physics*, *118*(7), 3937–3945. https://doi.org/10.1002/jgra.50337

Wang, X., Schwan, J., Hsu, H.-W., Grün, E., & Horányi, M. (2016). Dust charging and transport on airless planetary bodies. *Geophysical Research Letters*, *43*(12), 6103–6110. https://doi.org/10.1002/2016gl069491

Warell, J. (2004). Properties of the hermean regolith: IV. Photometric parameters of Mercury and the moon contrasted with Hapke modelling. *Icarus*, *167*(2), 271–286. https://doi.org/10.1016/j.icarus.2003.10.010

Wei, D., Wang, J., Nie, J., & Zhou, B. (2018). Generation of realistic sand particles with fractal nature using an improved spherical harmonic analysis. *Computers and Geotechnics*, *104*, 1–12. https://doi.org/10.1016/j.compgeo.2018.08.002

Wieser, M., Barabash, S., Futaana, Y., Holmström, M., Bhardwaj, A., Sridharan, R., et al. (2009). Extremely high reflection of solar wind protons as neutral hydrogen atoms from regolith in space. *Planetary and Space Science*, *57*(14–15), 2132–2134. https://doi.org/10.1016/j.pss.2009.09.012

Wood, S. E. (2020). A mechanistic model for the thermal conductivity of planetary regolith: 1. The effects of particle shape, composition, cohesion, and compression at depth. *Icarus*, *352*, 113964. https://doi.org/10.1016/j.icarus.2020.113964

Wurz, P., Fatemi, S., Galli, A., Halekas, J., Harada, Y., Jäggi, N., et al. (2022). Particles and photons as drivers for particle release from the surfaces of the Moon and Mercury. *Space Science Reviews*, *218*(3), 1–83. https://doi.org/10.1007/s11214-022-00875-6

Wurz, P., Rohner, U., Whitby, J. A., Kolb, C., Lammer, H., Dobnikar, P., & Martín-Fernández, J. (2007). The lunar exosphere: The sputtering contribution. *Icarus*, *191*(2), 486–496. https://doi.org/10.1016/j.icarus.2007.04.034

Yeo, L. H., Wang, X., Deca, J., Hsu, H.-W., & Horányi, M. (2021). Dynamics of electrostatically lofted dust on airless planetary bodies. *Icarus*, *366*, 114519. https://doi.org/10.1016/j.icarus.2021.114519

Yokota, S., Terada, N., Matsuoka, A., Murata, N., Saito, Y., Delcourt, D., et al. (2021). In situ observations of ions and magnetic field around phobos: The mass spectrum analyzer (MSA) for the Martian moons eXploration (MMX) mission. *Earth Planets and Space*, *73*(1), 1–18. https://doi.org/10.1186/s40623-021-01452-x

Zhang, A., Wieser, M., Wang, C., Barabash, S., Wang, W., Wang, X., et al. (2020). Emission of energetic neutral atoms measured on the lunar surface by Chang'E-4. *Planetary and Space Science*, *189*, 104970. https://doi.org/10.1016/j.pss.2020.104970

Ziegler, J. F., Ziegler, M. D., & Biersack, J. P. (2010). SRIM–The stopping and range of ions in matter (2010). *Nuclear Instruments and Methods in Physics Research Section B: Beam Interactions with Materials and Atoms*, *268*(11–12), 1818–1823. https://doi.org/10.1016/j.nimb.2010.02.091